Journal of Solid State Chemistry **156,** 117–121 (2001)
doi:10.1006/jssc.2000.8970, available online at http://www.idealibrary.com on IDEAL®

Internal Chemical Pressure Effect and Magnetic Properties of $La_{0.6}(Sr_{0.4-x}Ba_x)MnO_3$

C. H. Shen,* C. C. Chen,* R. S. Liu,*,[1] R. Gundakaram,* S. F. Hu,† and J. M. Chen‡

*Department of Chemistry, National Taiwan University, Taipei, Taiwan, Republic of China; †National Nano Device Laboratories, Hsinchu, Taiwan, Republic of China; and ‡Synchrotron Radiation Research Center, Hsinchu, Taiwan, Republic of China

Received May 16, 2000; in revised form August 10, 2000; accepted September 15, 2000; published online December 21, 2000

The effect of isovalent chemical substitution of Ba^{2+} into the Sr^{2+} sites on the structural and magnetic transition in $La_{0.6}(Sr_{0.4-x}Ba_x)MnO_3$ ($x = 0$–0.4) has been investigated. The rhombohedral structure with space group $R-3c$ is observed in this series of materials. Substitution of Sr and Ba in the La site changes the structural parameters such as the Mn–O bond lengths, thus allowing the study of the effect of the structure on magnetic properties. An increase in the Mn–O bond distance with increasing Ba content leads to a decrease in T_C (the temperature of the paramagnetic to ferromagnetic transition). © 2001 Academic Press

Key Words: **$La_{0.6}(Sr_{0.4-x}Ba_x)MnO_3$; internal chemical pressure; chemical substitution; colossal magnetoresistance; paramagnetic transition; ferromagnetic transition.**

INTRODUCTION

Rare-earth manganites have been the subject of considerable investigation since the discovery of their colossal magnetoresistance (CMR) properties (1, 2). Hole-doped manganites $(R_{1-x}M_x)MnO_3$ (R = trivalent lanthanide; M = divalent alkaline earth cation) with the perovoskite structure have been known to be an interesting class of materials. These materials exhibit a transition from a paramagnetic insulator to a ferromagnetic metal as the temperature is decreased, accompanied by a maximum in the electrical resistivity at a temperature T_m, which is close to the Curie temperature T_C. When a magnetic field is applied, the resistivity decreases and T_m shifts to higher temperatures. This phenomenon is the CMR effect, which has been explained by the double-exchange interactions resulting from the electron (hole) transfer between Mn^{3+} ($t_{2g}^3e_g^1$) and Mn^{4+} ($t_{2g}^3e_g^0$) with strong on-site Hund's coupling (3). The CMR behavior in manganites is closely related to the magnetic exchange interactions between two magnetic cations separated by an anion. Much of the efforts to improve the CMR effect at low fields and higher temperatures, which are very important for the practical application of these materials in devices, have been focused on the La-based manganites. As a function of temperature, effective ionic radius $\langle r_A \rangle$ of preovskite ABO_3 structure, Mn site disorder, applied magnetic field, applied pressure, or internal chemical pressure, this system displays a rich variety of properties (4–11). An increase in the paramagnetic to ferromagnetic transition temperature (T_C) with x and reaching a maximum ($\sim$370 K) around $x = 0.4$ was observed in $La_{1-x}Sr_xMnO_3$ (12). Moreover, the crystal structure of $La_{1-x}Sr_xMnO_3$ at room temperature changes from orthorhombic (*Pbnm*, $Z = 4$; $x < 0.175$) to rhombohedral ($R-3c$, $Z = 2$; $x \geq 0.175$) (12). The chemical substitution of Sr^{2+} for La^{3+} in $La_{1-x}Sr_xMnO_3$ increases the Mn valence with increasing Sr content. The largest influence on the structure is the overall amount of Mn^{4+} as pointed out by van Roosmalen *et al.* (13). With increasing Mn^{4+}, the unit cell volume decreases and the symmetry changes. With a low Mn^{4+} content an orthorhombic symmetry with a rather large deviation from the ideal perovskite structure has been observed, which is due to ordering of the Jahn–Teller distorted $Mn^{3+}O_6$ octahedra. The ordering is destroyed by an increase in the Mn^{4+} content, resulting in rhombohedral symmetry with a large Mn^{4+} content. While the T_C is close to room temperature in Ba-doped $LaMnO_3$ (e.g., $La_{1-x}Ba_xMnO_3$) (14), it is above room temperature in Sr-doped $LaMnO_3$ (2, 4). The gradual replacement of Ca by Ba in $La_{0.67}(Ca_{0.33-x}Ba_x)MnO_3$ (14) results in an increase in T_C from $\sim$265 K at $x = 0$ to $\sim$340 K at $x = 0.33$. The phase transformation from orthorhombic to rhombohedral, which has been observed in the $La_{0.67}(Ca_{0.33-x}Ba_x)MnO_3$ system with fixed Mn valence, is difficult to explain as the effect of increasing the Mn valence.

In this paper, we present our studies on the effect of doping Ba^{2+} into the Sr^{2+} site in $La_{0.6}Sr_{0.4}MnO_3$. We also demonstrate the relationship between the Mn–O bond

[1] To whom correspondence should be addressed. E-mail: rsliu@ccms.ntu.edu.tw. Fax: 886-2-23636359.

0022-4596/01 $35.00

lengths and T_C in the series of $La_{0.6}(Sr_{0.4-x}Ba_x)MnO_3$, which leads us to explore the cation size effects in CMR materials.

EXPERIMENTAL

Polycrystalline $La_{0.6}(Sr_{0.4-x}Ba_x)MnO_3$ samples with $0 \leq x \leq 0.4$ were prepared by the standard solid-state reaction method. High-purity powders of La_2O_3, $SrCO_3$, $BaCO_3$, and MnO_2 were mixed and calcined in air at 900°C for 24 h. The samples were then sintered in air at 1400°C for 24 h, at 1500°C for 24 h, and again at 1500°C for 24 h with an intermediate grinding after each heating step. Powder X-ray diffraction analyses were carried out with a SCINTAG (X1) diffractometer (Cu$K\alpha$ radiation, $\lambda = 1.5406$ Å) at 40 kV and 30 mA. Data for the Rietveld refinement were collected in the 2θ range 20°–120° with a step size of 0.02° and a count time of 10 s per step. The GSAS program (15) was used for the Rietveld refinement in order to obtain the information about the crystal structures of $La_{0.6}(Sr_{0.4-x}Ba_x)MnO_3$. Electron diffraction (ED) and high-resolution transmission electron microscopy (HRTEM) were carried out using a JEOL 4000EX electron microscope operated at 400 kV. The samples for the microscopy were dispersed in alcohol before being transferred to the carbon-coated copper grids.

The valence of Mn was determined by the X-ray absorption technique. The X-ray absorption experiments were carried out at the Synchrotron Radiation Research Center (SRRC) in Taiwan with an electron beam energy of 1.5 GeV and a maximum stored current of 240 mA. The spectra were recorded by measuring the sample current. The incident photon flux (I_o) was monitored simultaneously by using a Ni mesh located after the exit slit of the monochromator. All the measurements were performed at room temperature. Two cycles of runs were performed for each sample. The reproducibility of the absorption spectra of the same sample in different experimental runs was found to be extremely good. The photon energies were calibrated to an accuracy of 0.1 eV via the known O K-edge absorption peaks of CuO. The valence of Mn was also determined by chemical titration. The samples were dissolved in an excess of 20 ml of $K_2C_2O_4$ and 2 ml of H_2SO_4 around 65°C maintained by a water bath to reduce all Mn^{n+} to Mn^{2+} ($3 < n \leqq 4$), and then the excess $C_2O_4^{2-}$ ions in the solution were determined by titration at 65°C with a standard solution of $KMnO_4$ (16). Magnetization data were collected using a superconducting quantum interference device (SQUID) magnetometer (Quantum Design).

RESULTS AND DISCUSSION

The powder XRD patterns of the $La_{0.6}(Sr_{0.4-x}Ba_x)MnO_3$ ($0 \leq x \leq 0.4$) samples are shown in Fig. 1. Each composition of the series was of single phase. The peaks in each pattern can be indexed on the basis of a rhombohedral unit cell (space group, R-3c). A typical example of the observed and calculated diffraction profiles of the sample with $x = 0.2$ is shown in Fig. 2. The cell symmetry was identified by the observation of the reflection based on the limiting condition on hkl: $-h + k + l = 3n$, with the R centering of the unit cell which is consistent with the results of the XRD refinement as shown in Fig. 2. The structural parameters of the $La_{0.6}(Sr_{0.4-x}Ba_x)MnO_3$ compounds at room temperature are listed in Table 1. Due to

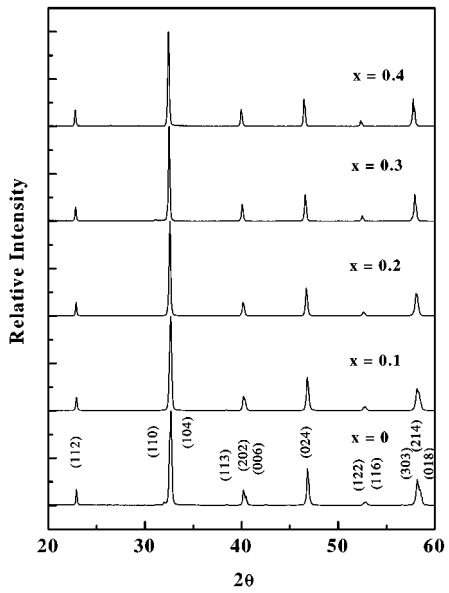

FIG. 1. XRD patterns of $La_{0.6}(Sr_{0.4-x}Ba_x)MnO_3$ ($0 \leq x \leq 0.4$).

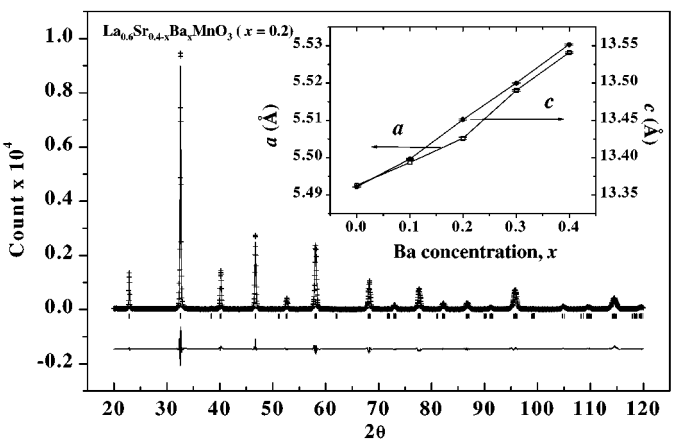

FIG. 2. Rietveld plot of $La_{0.6}(Sr_{0.4-x}Ba_x)MnO_3$ with $x = 0.2$ at 300 K. The experimental data points are shown as plus signs. The solid line is the calculated profile. The tic marks below the profile indicate the positions of allowed Bragg reflections. The difference plot (observed minus calculated) is shown at the bottom. The inset shows the variation of the cell parameters (a and c) as a function of x.

TABLE 1

Refined Fractional Atomic Positions, Unit Cell, and Reliability Factors (%) of $La_{0.6}(Sr_{0.4-x}Ba_x)MnO_3$ ($0 \le x \le 0.4$) Having *R*-3*c* Space Group at Room Temperature

	$x = 0$	$x = 0.1$	$x = 0.2$	$x = 0.3$	$x = 0.4$
R,*M* $10^2 u_{iso}$(Å^2)	1.58(3)	1.56(3)	1.31(2)	1.63(3)	1.93(4)
Mn $10^2 u_{iso}$(Å^2)	1.36(4)	1.19(4)	0.97(4)	1.89(5)	1.78(7)
O *x*	0.5415(9)	0.5345(9)	0.533(1)	0.531(1)	0.526(1)
$10^2 u_{iso}$(Å^2)	2.2(1)	2.1(1)	2.4(1)	2.6(2)	2.4(2)
a (Å)	5.4926(3)	5.4987(3)	5.5052(3)	5.518(2)	5.5282(2)
b (Å)	5.4926(3)	5.4987(3)	5.5052(3)	5.518(2)	5.5282(2)
c (Å)	13.3609(7)	13.3982(7)	13.451(1)	13.50(1)	13.552(1)
Volume (Å^3)	349.08(3)	350.83(3)	353.04(3)	355.9(3)	358.66(4)
R_p (%)	9.72	9.15	9.54	9.61	10.43
R_{wp} (%)	12.95	12.41	13.01	13.03	13.92
χ^2 (%)	2.243	1.756	1.603	1.601	1.834
Mn–O (Å)	1.9508(6)	1.9499(5)	1.9529(5)	1.9575(7)	1.9601(7)
Mn–O–Mn	180°	180°	180°	180°	180°
r_A (Å)	1.254	1.270	1.286	1.302	1.318
t_{factor}	0.939	0.945	0.950	0.956	0.961
T_C (K)	380	375	370	360	350

Note. The atomic positions are *R*,*M* (La, Sr, and Ba atoms), (0, 0, 0.25); Mn, (0, 0, 0); O, (*x*, 0, 0.25). The corresponding t_{factor} and T_C values are also given.

the rhombohedral crystal structure of $La_{0.6}Sr_{0.4}MnO_3$ and $La_{0.6}Ba_{0.4}MnO_3$, there would be no distortion in the MnO_6 octahedra at room temperature. Therefore, an increase in the Ba content in $La_{0.6}Sr_{0.4}MnO_3$ would lead to an increase in the bond lengths of the MnO_6 octahedra. The lattice constants *a* and *c* increase as the Ba (*x*) content increases (as shown in the inset of Fig. 2). This is due to a manifestation of the bigger size of the substituting Ba^{2+} ion [1.47 Å for *C.N.* (coordination number) = 9] as compared to the smaller Sr^{2+} ions (1.31 Å for *C.N.* = 9) (17). In Fig. 3, the dependence of the cell volume and Mn–O bond distances on the effective ionic radius of the A-site $\langle r_A \rangle$ is shown. The enlargement of the Mn–O (along each direction of the MnO_6 octahedra) bond distance is consistent with an increase in the cell volume. Moreover, an increase in the tolerance factor (t_{factor}) with increasing Ba doping was found (as shown in Table 1). The tolerance factor is defined as $(r_A + r_o)/\sqrt{2}(r_B + r_o)$, where r_A, r_B, and r_o are the ionic radii of the *A*, *B* cations and oxygen, respectively, in the perovskite ABO_3 structure. The $t_{factor} = 1$ for the compound with an ideal perovskite structure. If $t_{factor} < 1$, the strain within the compound is increased. Therefore, the t_{factor} increases (from 0.939 for $x = 0$ to 0.961 for $x = 0.4$) with the addition of Ba giving rise to the release of the strain for $La_{0.6}(Sr_{0.4-x}Ba_x)MnO_3$.

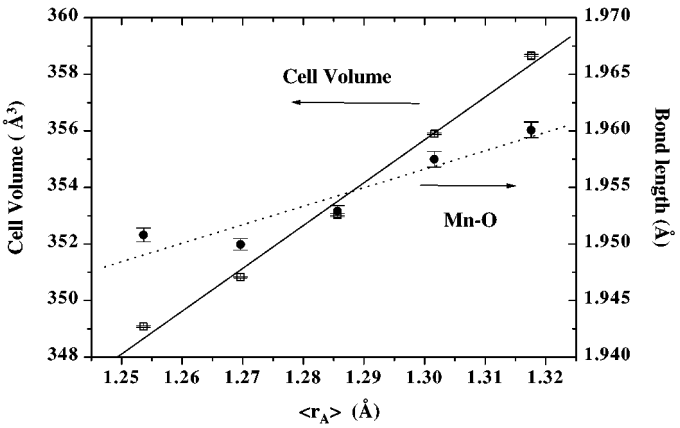

FIG. 3. Mn–O bond distances and cell volume as a function of the effective ionic radius $\langle r_A \rangle$ of $La_{0.6}(Sr_{0.4-x}Ba_x)MnO_3$.

The HRTEM atomic images along [001] and [010] of zone-axis directions of the $La_{0.6}(Sr_{0.4-x}Ba_x)MnO_3$ sample with $x = 0.1$ are shown in Figs. 4a and 4b, respectively. The corresponding electron diffraction patterns are shown in the insets of Figs. 4a and 4b. The cell symmetry was identified to be rhombohedral by the observation of the reflections based on the limiting condition on *hkl*: $-h + k + l = 3n$, with the *R* centering of the unit cell.

The Mn 2*p*-edge X-ray absorption near edge structure (XANES) spectra of the compositions $La_{0.6}(Sr_{0.4-x}Ba_x)MnO_3$ ($0 \le x \le 0.4$) are shown in Fig. 5. As can be seen from this figure, the spectra show two broad multiple structures separated by spin–orbit splitting ($Mn2p_{3/2}$ and $Mn2p_{1/2}$). The chemical shift is caused by changes in the electrostatic energy at the Mn site driven by the variation of the ionic valence in the compounds. It is well established that the effective ionic valence of the compounds can be measured from the chemical shift of the core-level X-ray photoemission (18–20). We, therefore, adopt the same scheme and determine the Mn valence to be around 3.43 ± 0.05 across the series $La_{0.6}(Sr_{0.4-x}Ba_x)MnO_3$ for $0 \le x \le 0.4$. Moreover, the Mn valence of all the samples as determined by chemical titration is also around 3.42 ± 0.04.

In Fig. 6, we show the temperature dependence of magnetization at a magnetic field of 0.1 T for the series $La_{0.6}(Sr_{0.4-x}Ba_x)MnO_3$ ($0 \le x \le 0.4$). In the temperature range 380–350 K, a paramagnetic to ferromagnetic transition is observed in the series. A decrease in T_C from 380 K of $x = 0$ to 350 K of $x = 0.4$ was observed. This suggests that the bigger Ba^{2+} ions substitute the smaller Sr^{2+} sites, leading to a decrease in the T_C. Based on the model of double exchange, a lower T_C corresponds to a poor overlap between Mn3*d* and O2*p* orbitals, resulting in a reduced bandwidth (*W*) (4). The following empirical formula has been used to describe the variation of bandwidth (*W*) in the double-exchange mechanism of manganites,

$$W \propto \cos\omega / d_{Mn-O}{}^{3.5},$$

where ω is the tilt angle in the plane of the bond [$\omega = 180° - \alpha$; α is the angle of Mn–O–Mn] and d_{Mn-O} is

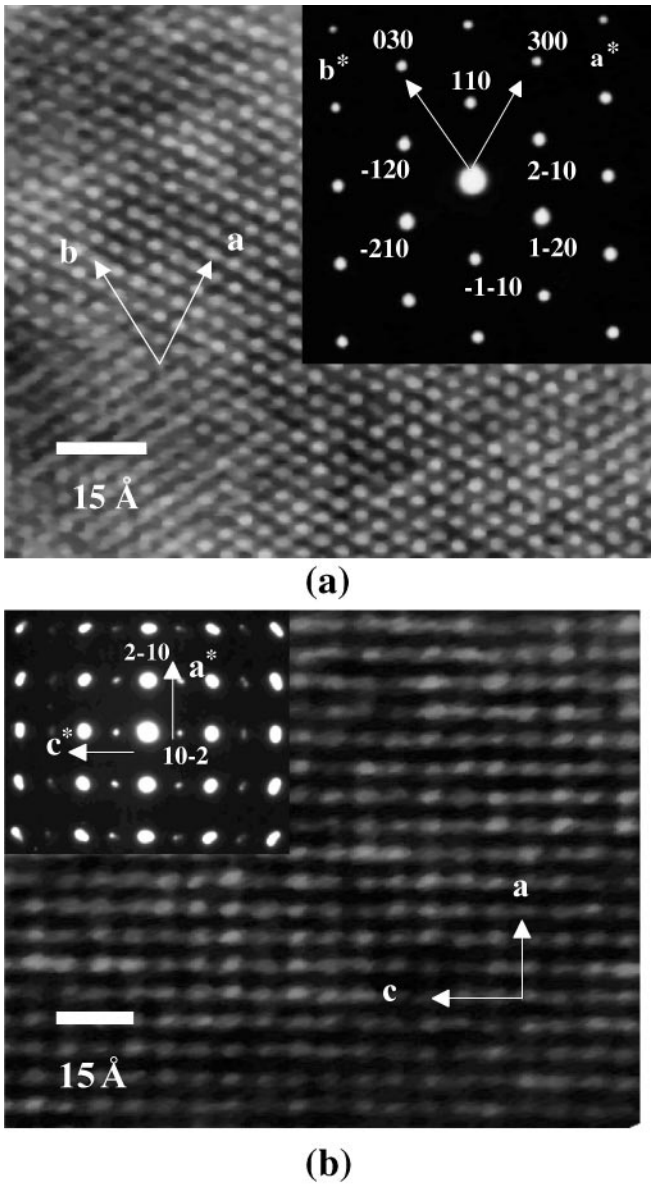

FIG. 4. HRTEM lattice images recorded along the (a) [001] and (b) [010] zone-axis directions of the $La_{0.6}(Sr_{0.4-x}Ba_x)MnO_3$ sample with $x = 0.1$. The corresponding electron diffraction patterns are shown in the insets.

the Mn–O bond length. With increasing x, the Mn–O–Mn bond angle remains unchanged (as can be seen from Table 1) and the increase of Mn–O bond length (as shown in Fig. 3) contributes to the decrease of W, which results in the decrease in T_C. The increase in the Mn–O bond length reduces the overlap between the Mn3d and O2p orbitals. Thus, the chemical substitution of isovalent Ba for Sr leads to poor hybridization between the orbitals in the rhombohedral cell, causing a decrease in T_C.

In conclusion, this study has demonstrated that doping of Ba^{2+} in the Sr^{2+} site releases internal chemical pressure and also decreases T_C. Therefore, the effective ionic radius of the A-site, which can be varied by tuning the concentration of Ba^{2+} and Sr^{2+}, plays an important role in controlling the crystal structural and T_C in the series $La_{0.6}(Sr_{0.4-x}Ba_x)MnO_3$.

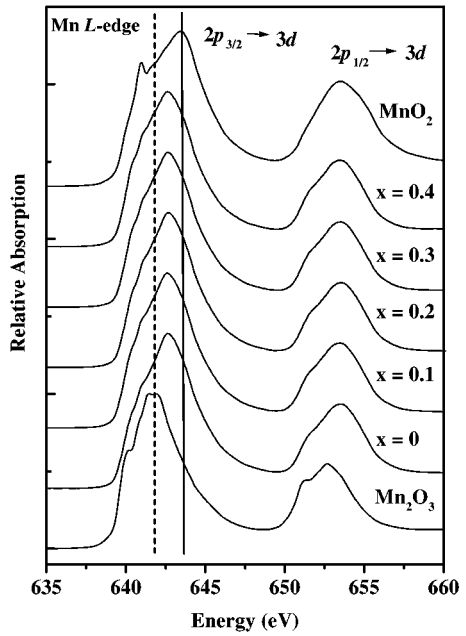

FIG. 5. Mn 2p-edge X-ray absorption near-edge structure (XANES) spectra of samples with nominal composition of $La_{0.6}(Sr_{0.4-x}Ba_x)MnO_3$ and those of two standards, MnO_2 (Mn^{4+}) and Mn_2O_3 (Mn^{3+}).

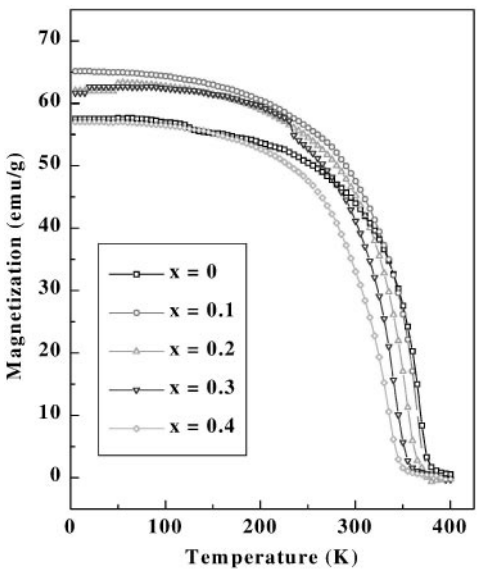

FIG. 6. Temperature dependence of magnetization (emu/g vs T) in an applied magnetic field of 0.1 T of the $La_{0.6}(Sr_{0.4-x}Ba_x)MnO_3$.

ACKNOWLEDGMENTS

This research has been financially supported by the National Science Council of the Republic of China under grant number NSC 89-2113-M-002-004.

REFERENCES

1. P. R. Broussard, S. B. Qadri, V. M. Browning, and V. C. Cestone, *J. Appl. Phys.* **85,** 6563 (1999).
2. F. Bridges, C. H. Booth, G. H. Kwei, J. J. Neumeier, and G. A. Sawatzky, *Phys. Rev. B* **61,** R9237 (2000).
3. C. Zener, *Phys. Rev.* **82,** 403 (1951).
4. P. G. Radaelli, G. Iannone, M. Marezio, H. Y. Hwang, S.-W. Cheong, J. D. Jorgensen, and D. N. Argyriou, *Phys. Rev. B* **56,** 8265 (1997).
5. L. M. Rodriguez-Martinez, H. Ehrenberg, and J. P. Attfield, *J. Solid State Chem.* **148,** 20 (1999).
6. C. N. R. Rao, P. N. Santhosh, R. S. Singh, and A. Arulraj, *J. Solid State Chem.* **135,** 169 (1998).
7. R. Mahendiran, S. K. Tiwary, A. K. Raychaudhuri, T. V. Ramakrishnan, R. Mahesh, N. Rangavittal, and C. N. R. Rao, *J. Solid State Chem.* **114,** 297 (1995).
8. K. Hirota, A. Nishizawa, and. Y. Endoh, *J. Magn. Magn. Mater.* **197–181,** 864 (1998).
9. Z. B. Guo, Y. W. Du, J. S. Zhu, H. Huang, W. P. Ding, and D. Feng, *Phys. Rev. Lett.* **78,** 1142 (1997).
10. H. Y. Hwang, S.-W. Cheong, P. G. Radaelli, M. Marezio, and B. Batlogg, *Phys. Rev. Lett.* **75,** 914 (1995).
11. R. Mahesh, R. Mahendiran, A. K. Raychaudhuri, and C. N. R. Rao, *J. Solid State Chem.* **120,** 204 (1995).
12. A. Urushibara, Y. Moritomo, T. Arima, A. Asamitsu, G. Kido, and Y. Tokura, *Phys. Rev. B* **51,** 14103 (1995).
13. J. A. M. van Roosmalen, P. van Vlaanderen, and E. H. P. Cordfunke, *J. Solid State Chem.* **114,** 516 (1995).
14. N. Moutis, I. Panagiotopoulos, M. Pissas, and D. Niarchos, *Phys. Rev. B* **59,** 1129 (1999).
15. A. C. Larson and R. B. von Dreele, "Generalized Structure Analysis System." Los Alamos National Laboratory, Los Alamos, NM, 1994.
16. M. J. Katz, R. C. Charke, and W. F. Nye, *Anal. Chem.* **28,** 507 (1956).
17. R. D. Shanon, *Acta Crystallogr. Sect. A* **32,** 751 (1976).
18. M. Abbate, F. M. F. de Groot, J. C. Fuggle, A. Fujimori, O. Strebel, F. Lopez, M. Domke, G. Kaindl, G. A. Sawatzky, M. Takano, Y. Takeda, H. Eisaki, and S. Uchida, *Phys. Rev. B* **46,** 4511 (1992).
19. D. D. Sarma, O. Rader, T. Kachel, A. Chainani, M. Mathew, K. Holldack, W. Gudat, and W. Eberhardt, *Phys. Rev. B* **49,** 14238 (1994).
20. G. Zampieri, F. Prado, A. Caneiro, J. Briatico, M. T. Causa, M. Tovar, B. Alascio, M. Abbate, and E. Morikawa, *Phys. Rev. B* **58,** 3755 (1998).